ARTICLES
https://doi.org/10.1038/s41563-020-0753-1

nature materials

Finned zeolite catalysts

Heng Dai[1,6], Yufeng Shen[1,6], Taimin Yang[2], Choongsze Lee[3], Donglong Fu[4], Ankur Agarwal[1], Thuy Thanh Le[1], Michael Tsapatsis[3,5], Jeremy C. Palmer[1], Bert M. Weckhuysen[4], Paul J. Dauenhauer[3], Xiaodong Zou[2] and Jeffrey D. Rimer[1]✉

There is growing evidence for the advantages of synthesizing nanosized zeolites with markedly reduced internal diffusion limitations for enhanced performances in catalysis and adsorption. Producing zeolite crystals with sizes less than 100 nm, however, is non-trivial, often requires the use of complex organics and typically results in a small product yield. Here we present an alternative, facile approach to enhance the mass-transport properties of zeolites by the epitaxial growth of fin-like protrusions on seed crystals. We validate this generalizable methodology on two common zeolites and confirm that fins are in crystallographic registry with the underlying seeds, and that secondary growth does not impede access to the micropores. Molecular modelling and time-resolved titration experiments of finned zeolites probe internal diffusion and reveal substantial improvements in mass transport, consistent with catalytic tests of a model reaction, which show that these structures behave as pseudo-nanocrystals with sizes commensurate to that of the fin. This approach could be extended to the rational synthesis of other zeolite and aluminosilicate materials.

The confined channels and cages of microporous materials (zeolites) are utilized in numerous applications, which span from catalysis[1,2] and adsorption[3] to selective separations[4,5]. A common objective in the design of zeolitic materials is to overcome the inherent mass-transport limitations of micropores. This is a ubiquitous challenge for the development of zeolite catalysts in which narrow pore apertures and long diffusion path lengths lead to more rapid deactivation owing to the accumulation of carbonaceous deposits (coke)[6]. This is particularly true for zeolites with low-dimensional pore networks. There is an increasing body of literature that shows how the preparation of nanosized crystals can enhance catalyst lifetime and/or alter product selectivity[7,8]. For example, the advent of two-dimensional (2D)[9,10] or self-pillared[11] zeolites with sizes on the order of a crystal unit cell (~2–4 nm) exhibit a superior catalytic performance to that of conventional zeolites; however, the preparation of these materials has only been demonstrated for a few framework types. Indeed, only a relatively small number of reported zeolites have crystal sizes less than 100 nm (refs. [12–14]), which highlights the challenges associated with synthesizing nanosized microporous materials. This has motivated the development of alternative methods, such as the preparation of hierarchical zeolites[15,16], in which the introduction of mesopores has an analogous beneficial effect on mass transport[17,18]. The practical challenges of nanosized zeolite synthesis include the customary requirement of unconventional organics and the frequent drawback of small product yields. This underscores the need for more facile, efficient methods to produce nanosized zeolites by methodologies that are generalizable to a broad number of framework types.

One-pot synthesis of finned zeolites

Here we investigate an alternative method to reduce internal diffusion limitations via the synthesis of zeolites with rough protrusions (size α) on their exterior surfaces (Fig. 1a), which exhibit an identical crystallographic registry with the interior crystal (size β). These features resemble 'fins', which are well-known to enhance the rate of heat transfer in conductive materials owing to the increased external surface area. Analogous to studies by Ryoo and co-workers[10], who showed that hierarchical zeolites that possess a high external surface area markedly reduce external coking, we demonstrate a similar effect for finned catalysts, and focus on two common 3D medium-pore zeolites: ZSM-11 (MEL framework) and ZSM-5 (MFI framework). The synthesis of ZSM-11 by a previously reported protocol[19] yields crystals with relatively smooth exterior surfaces (Supplementary Fig. 1). We identified an alternative one-pot synthesis of ZSM-11 that produces crystals with finned surfaces (Fig. 1b,c). Transmission electron microscopy (TEM) reveals that these are single crystals (Fig. 1d) with an identical registry between the centre of the particle and the exterior fins. These exterior features are aligned in parallel with an average dimension of 35 nm (Fig. 1e). Elemental analysis reveals no evidence of aluminium zoning (Supplementary Table 1)[20], which has been reported for ZSM-5[21]. Moreover, textural analysis (Supplementary Fig. 2) shows no evidence of mesoporosity in ZSM-11 samples, although TEM tomography reveals the presence of isolated pores within the interior of these particles (Supplementary Fig. 3 and Supplementary Video 1), which is probably attributable to the non-classical mechanism of zeolite growth that involves particle attachment[22,23].

Prior studies have reported rough crystals of ZSM-11[24] and ZSM-5[25]. The majority of these examples are structures with distinctly different features to those reported here. Notably, the rough crystals reported in literature are commonly aggregates with small crystallites arranged in random orientations on the exterior surfaces of larger particles (Supplementary Fig. 4). These misoriented domains can give rise to pore blockage at the interfacial boundaries between adjacent particles; however, prior studies have demonstrated that these aggregated structures enhance the overall catalytic performance relative to that of conventional analogues, which is attributed to the introduction of interstitial mesopores[26]. Here we show that the one-pot synthesis of finned ZSM-11 improves the catalyst properties

[1]Department of Chemical and Biomolecular Engineering, University of Houston, Houston, TX, USA. [2]Department of Materials and Environmental Chemistry, Stockholm University, Stockholm, Sweden. [3]Department of Chemical Engineering and Materials Science, University of Minnesota, Minneapolis, MN, USA. [4]Inorganic Chemistry and Catalysis Group, Debye Institute for Nanomaterials Science, Utrecht University, Utrecht, the Netherlands. [5]Department of Chemical and Biomolecular Engineering, Johns Hopkins University, Baltimore, MD, USA. [6]These authors contributed equally: Heng Dai, Yufeng Shen. ✉e-mail: jrimer@central.uh.edu

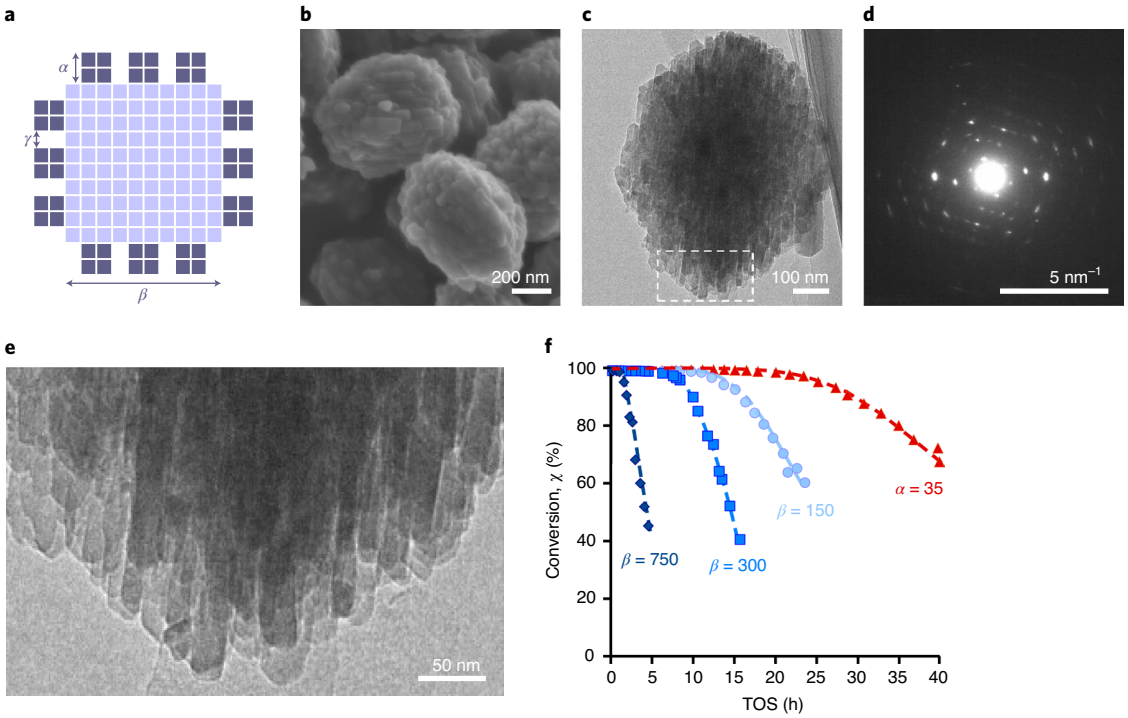

Fig. 1 | One-pot preparation of finned ZSM-11. a, Idealized schematic of a finned zeolite with fin and interior dimensions of α and β, respectively, and fin pitch γ. **b**, Scanning electron micrograph of zeolite ZSM-11 crystals with finned surfaces prepared from a one-pot synthesis (Supplementary Table 2). **c**, Transmission electron micrograph of a representative finned ZSM-11 crystal. **d**, Corresponding SAED pattern of the crystal in **c** showing a single-crystal pattern behaviour. **e**, High-magnification TEM image from **c** (dashed box) showing the parallel alignment of fins. **f**, TOS MTH conversion for H-ZSM-11 catalysts (Si/Al ≈ 20) at 350 °C with WHSV = 9 h^{-1}. The performance of finned H-ZSM-11 with an overall size of 460 nm ($\alpha \approx 35$ nm) (triangles) is compared with conventional H-ZSM-11 crystals (Supplementary Table 2) with sizes of 750 nm (diamonds), 300 nm (squares) and 150 nm (circles). Dashed lines are interpolations to guide the eye.

owing to a different mechanism: enhanced mass transport through fins of a much smaller dimension (that is, $\alpha << \beta$). Shen et al.[19] previously reported trends in catalyst lifetime and selectivity as a function of H-ZSM-11 crystal size (150, 300 and 750 nm) using methanol-to-hydrocarbons (MTH) as a model reaction. In Fig. 1f, the time-on-stream (TOS) conversions over these three catalysts are compared with that of the finned H-ZSM-11 sample, which has an overall size of ~460 nm, fins included. Interestingly, the finned catalyst deviates from the trend of increasing lifetime with decreasing crystal size when comparisons are made on the basis of overall particle dimension; however, the trend is qualitatively consistent if the finned catalyst behaves as a crystal of much smaller size, commensurate with that of the average fin dimension ($\alpha \approx 35$ nm).

Preparation of finned zeolites by secondary growth

The preparation of finned zeolite crystals via a one-pot synthesis is arbitrary and difficult to predict owing to the largely unknown impact of synthesis parameters on zeolite crystallization. To this end, secondary (or seeded) growth offers a more controlled method to create fins on the exterior surfaces of seed crystals. Here we demonstrate the secondary growth method for both ZSM-11 (Fig. 2a–d) and ZSM-5 (Fig. 2e–h). Scanning electron microscopy images of ZSM-11 (Fig. 2a) and ZSM-5 (Fig. 2e) seeds reveal exterior crystal surfaces devoid of rough features. Scanning electron microscopy images after secondary growth of ZSM-11 (Fig. 2b) and ZSM-5 (Fig. 2f) confirm the presence of fins (protrusions). TEM images show average feature sizes of 30 ± 3 nm for ZSM-11 (Fig. 2c) and 53 ± 6 nm for ZSM-5 (Fig. 2g). Selected area electron diffraction (SAED) patterns (Fig. 2d,h) also confirm that the samples are single zeolite crystals, which thus indicates that the fins grow epitaxially on the surfaces of the seeds. Powder X-ray diffraction (XRD) patterns indicate that the samples are fully crystalline before and after seeded growth (Supplementary Figs. 5 and 6), whereas textural analysis (Supplementary Table 3 and Supplementary Fig. 7) shows a slight increase in the total surface area (~8%) with secondary growth without an appreciable change in micropore volume (as shown in Supplementary Table 3, the micropore volumes for finned and seed particles are indistinguishable). Elemental analysis (Supplementary Table 3) also confirms that the Si/Al ratio of the samples before and after seeded growth are nearly identical.

The protocol to generate finned zeolites (Methods) was strategically selected by adjusting the supersaturation to a level that was sufficiently high to avoid layer-by-layer growth of core–shells (that is, complete overgrowth of seed crystals), which was previously demonstrated by Ghorbanpour et al.[27]. However, there is an upper limit of supersaturation that, when exceeded, leads to the homogeneous nucleation of new crystals in the growth solution, and thereby generates aggregates of both small and large crystallites. TEM tomography of finned ZSM-11 (Fig. 2i and Supplementary Video 2) and ZSM-5 (Fig. 2j and Supplementary Video 3) after secondary growth confirmed the absence of intraparticle mesoporosity. TEM tomograms of each sample perpendicular to the z direction (z stacks), depicted in Fig. 2i,j at the bottom, middle and top of the particles, clearly show the size and distribution of fins on the exterior surfaces. The finned zeolites prepared by secondary growth (Fig. 2k) comprise regions with two characteristic dimensions: β is the size of the original seed along the principal zone axis of diffusion (that is b directions for MFI and MEL) and α is the average size of the fins. An idealized schematic of finned zeolites (Fig. 2l) shows medium-pore channels that extend from the interior to exterior with an identical registry where the net increase in external surface area is highly

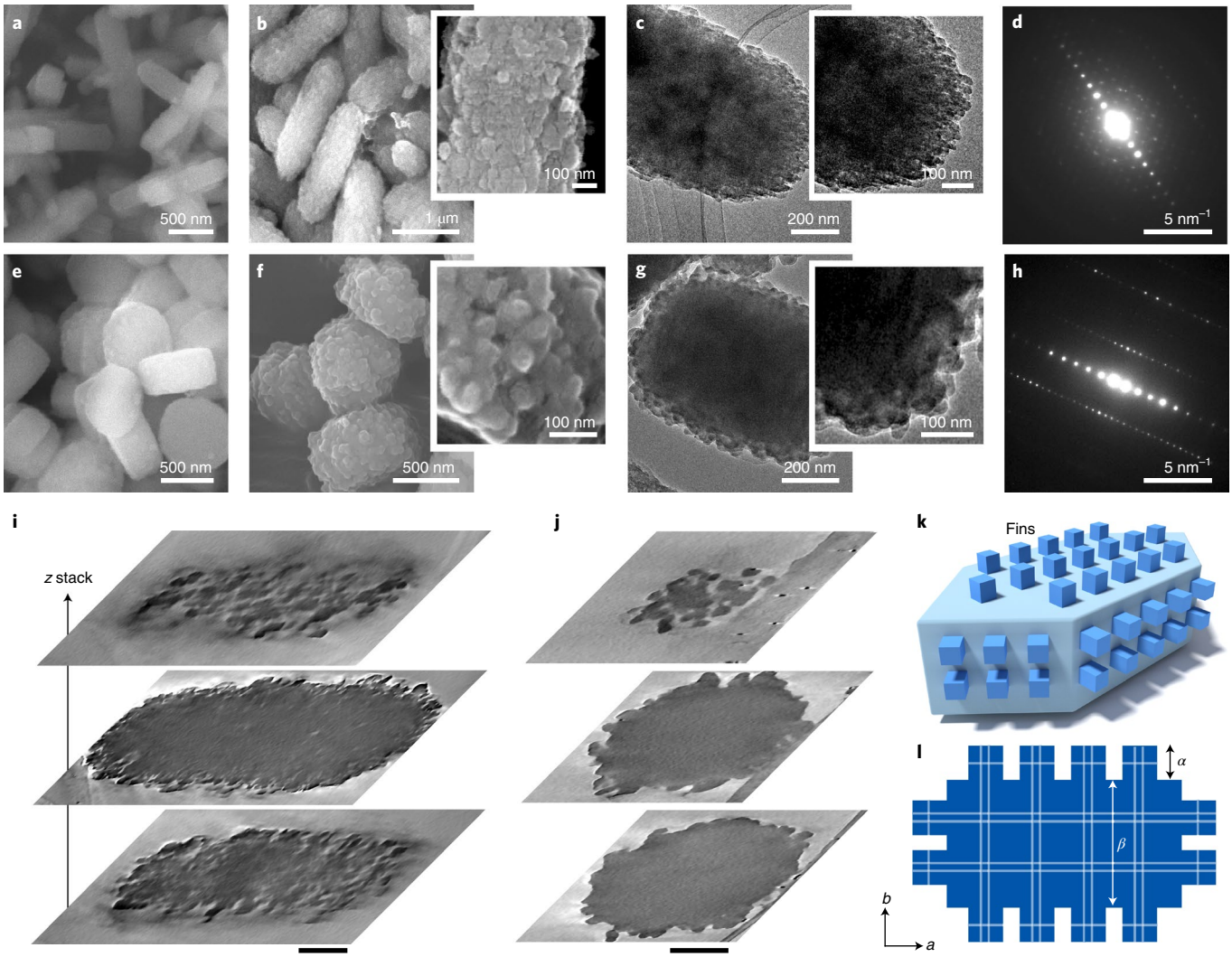

Fig. 2 | Seed-assisted preparation of finned ZSM-11 and ZSM-5. a–h, Electron micrographs of zeolite ZSM-11 (**a**–**c**) and ZSM-5 (**e**–**g**) crystals. Comparisons are made between seeds prepared by conventional protocols (**a** and **e**) and the finned crystals (**b**–**d** for ZSM-11 and **f**–**h** for ZSM-5) prepared by secondary growth of the seeds (Supplementary Table 4). SAED patterns (**d** and **h**) reveal that the finned zeolites are single crystals. **i**,**j**, TEM tomography images of finned ZSM-11 (**i**) and ZSM-5 (**j**) crystals showing cross-sectional images from Supplementary Videos 2 and 3, respectively. Scale bars, 200 nm. (**k**) Idealized schematic of a finned zeolite in which the fins have the same crystallographic registry as the seed. (**l**) Illustration of a finned zeolite that comprises continuous channels throughout the seed (size β) and fins (size α) with characteristic fin dimensions of $\alpha \times \alpha \times \alpha$, as indicated in the TEM images of ZSM-11 and ZSM-5.

dependent on the relative sizes of β and α (Supplementary Note 1 and Supplementary Fig. 8).

Impact of fins on catalyst performance

To substantiate the enhanced mass-transport properties of zeolites after secondary growth, we assessed the performance of the acid-exchanged (H-form) seed and finned samples in the MTH reaction at subcomplete methanol conversion (60–90%). The acid-site density and the framework Al of each catalyst was quantified (Supplementary Table 3 and Supplementary Fig. 9) to ensure a consistent weight hourly space velocity (WHSV). TOS analysis of both seed and finned H-ZSM-11 (Fig. 3a) and H-ZSM-5 (Fig. 3b) samples reveals similar catalyst activity (that is, a nearly identical starting conversion). This suggests that the reactions in finned samples are not solely restricted to the exterior protrusions, but also occur within the interior of the catalyst. This is qualitatively consistent with the TEM and textural analyses showing the epitaxial growth of fins without a noticeable obstruction of the pores at the fin–seed boundary. For both crystal topologies, we observed an approximate threefold reduction in the rate of deactivation, which thus confirms that the presence of fins markedly extends the catalyst lifetime. Moreover, comparison of the product selectivities (Fig. 3c,d) reveals a subtle shift whereby finned zeolites, which seemingly behave as pseudo nanocrystallites of dimension α, promote the olefin-based cycle of the MTH hydrocarbon pool (HCP) mechanism[28]. Prior studies showed a progressive shift in the preferred cycle (from aromatic to olefin) with decreasing crystal size[29]. This is clearly evident when the conventional descriptor ethylene/2MBu is compared, which is a ratio of the signature products from the aromatic-based cycle (ethylene) and olefin-based cycle (2MBu, 2-methylbutane and 2-methyl-2-butene). Over the entire range of the methanol conversion, we observed a noticeable reduction in the ethylene/2MBu ratio of finned catalysts (Fig. 3e), which agrees with the expected trend for smaller particles.

MTH reactions were repeated using operando ultraviolet–visible light (UV–vis) diffuse reflectance spectroscopy coupled with online

gas chromatography to track the spatiotemporal progression of the formation of hydrocarbon species in the zeolite crystals. It was previously shown[30] that a UV–vis spectrum obtained during MTH catalysis can be grouped into three distinct regions of wavelengths, which correspond to HCP species as well as to small and large polyaromatics. HCP species are reaction products small enough to diffuse through zeolite pores; small polyaromatics are associated with internal coke, given that their size is sufficiently large to fit within zeolite pores, but too large to diffuse out of the zeolite; and large polyaromatics are attributed to external coke. The UV–vis spectra for H-ZSM-11 (Fig. 3f) reveal equivalent internal coke between seed and finned samples; however, there is a noticeable reduction in the quantity of external coke for the finned sample, which suggests the presence of external protrusions leads to less accumulation of polyaromatics at the pore mouths. A similar trend was observed for H-ZSM-5 samples (Fig. 3g), but with a shorter lifetime owing to the tortuous sinusoidal channels of MFI compared to the straight channels of MEL (Fig. 3a,b, insets). Collectively, these studies indicate that finned catalysts enhance mass-transport properties of the zeolite by suppressing the formation of external coke. This seemingly implies that olefins and small aromatics more readily diffuse through the fins, which leads to reduced residence times of HCP species near the pore mouths.

One advantage of the finned synthesis approach is that it is theoretically applicable to a wide range of framework types. Moreover, this approach can be used to upgrade commercial catalysts via the addition of a secondary growth step. As proof of principle, we performed a seeded growth experiment using a commercial ZSM-5 sample from Zeolyst (CBV5524G, Si/Al = 25). Electron micrographs of the as-received H-ZSM-5 reveal a heterogeneous particle size distribution with dimensions that span 100–250 nm (Fig. 3h and Supplementary Fig. 12). Secondary growth of these particles successfully generated finned H-ZSM-5 with $\alpha = 35 \pm 5$ nm (Fig. 3i and Supplementary Fig. 12). Elemental analysis (Supplementary Table 5) also confirms that the Si/Al ratio of the samples before and after the seeded growth were nearly identical. MTH reactions at complete methanol conversion over as-received and finned catalysts reveal that the latter exhibits longer lifetime (Fig. 3j) with expected trends in product selectivity (Supplementary Fig. 13), analogous to the synthetic seed and finned samples. Note that the preparation of ZSM-5 with a high Al content (Si/Al = 15–25) and sizes ranging from 2 nm (2D materials) to 100 nm (commercial samples) is largely inaccessible by conventional synthesis routes; however, the synthesis of finned zeolites offers a unique route to achieve pseudo-crystallites within this largely inaccessible size range.

Mass-transport properties of finned zeolites

To confirm whether finned zeolites exhibit distinct mass-transport properties relative to conventional (seed) zeolites, we performed kinetic Monte Carlo (KMC) simulations to compare the diffusive behaviour of benzene (a relatively bulky, representative hydrocarbon molecule) in silicalite-1, the siliceous isostructure of ZSM-5, with preset α and β dimensions. The schematic in Fig. 1a, which is not drawn to full scale, is a cross-section of the 3D model used in the KMC simulations in which each square represents a unit cell of silicalite-1 (unit cells that belong to the seed and fins are coloured light and dark blue, respectively). The simulated model contains ~10^7 unit cells. Benzene diffuses through the pore network of silicalite-1 via a series of infrequent hops between favourable adsorption sites in the framework's straight pores (S), sinusoidal channels (Z) and at their intersections (I) (Fig. 4a–c), which can be described by first-order kinetics. The KMC simulations of benzene hopping dynamics in silicalite-1 using rate constants from molecular modelling yield diffusivity estimates (Supplementary Table 6) that are in good agreement with experiment[31,32]. We used this modelling approach to estimate the diffusion path length r, defined as the total trajectory length of a benzene molecule between first entrance and exit of the zeolite crystal, for seed and finned superstructures created by replication of the periodic MFI unit cell. For a seed crystal ($\beta = 500$ nm), the mean diffusion path length for benzene was $r = 138$ nm, which corresponds to a characteristic residence time of $\tau = 1.9 \times 10^{-5}$ s (Fig. 4d and Supplementary Table 7). When the surface was decorated with fins ($\alpha = 50$ nm) with a fixed pitch γ of 10 nm, we obtained $r = 58$ nm and $\tau = 7.9 \times 10^{-6}$ s (Fig. 4d and Supplementary Table 7). This 2.4-fold reduction arises from the comparatively shorter distance, relative to the seed crystal, required for diffusing molecules to enter and exit through the fins. Although the magnitude of the improvement depends on the fin surface density (Supplementary Table 7), KMC simulations show that the finned structures exhibit superior mass-transport characteristics, consistent with experimental observations.

The enhanced mass-transport properties of finned zeolites were further verified using an experimental protocol to assess internal diffusion based on time-resolved Fourier-transform infrared (FTIR) spectroscopy. In these studies, the purified bulky organic base 2,4,6-trimethylpyridine (TMPyr) was used to titrate Brønsted acid sites within zeolite micropores (see Supplementary Note 2 and Supplementary Fig. 14 for details). Diffusion and adsorption of TMPyr slowly permeated the micropores of H-ZSM-11 and H-ZSM-5 over 72 hours due to steric hindrance from the methyl groups[33]. The temporal permeation of TMPyr was quantified by the disappearance of FTIR intensity at 3,605 cm^{-1} which corresponds to the vacant Brønsted acid sites and also by the appearance of peaks at 1,565 cm^{-1} associated with the trimethylpyridinium ion (Supplementary Fig. 15). The loss of Brønsted acid sites is linearly correlated to the increase in trimethylpyridinium ions (Supplementary Fig. 16). The distinct TMPyr uptake kinetics for H-ZSM-11 (Fig. 4e) and H-ZSM-5 (Supplementary Fig. 17), both with and without fins, are described by an exponential diffusion model. When the differential of the titrated Brønsted acid sites over time was plotted for the Zeolyst samples (Fig. 4f) and other zeolites (Supplementary Fig. 18), we observed the two distinct diffusion regimes, which indicates the initial fast uptake of TMPyr in the fins relative to the bulk particle. To further assert the correspondence of the two timescales to the finned and bulk portions of the crystals, we also applied the method to examine

Fig. 3 | Superior performance of finned zeolite catalysts. a,**b**, Plots of subcomplete methanol conversion over zeolite H-ZSM-11 (**a**) and H-ZSM-5 (**b**) catalysts during MTH catalysis as a function of TOS. Comparisons are made between seed and finned samples during the MTH reaction at 350 °C with WHSV = 20 h^{-1}. Insets: schematics of MEL and MFI frameworks, respectively. The rate of catalyst deactivation (slope with units of h^{-1}) is labelled for each sample. **c**,**d**, Selectivities of hydrocarbon products for seed and finned H-ZSM-11 (**c**) and H-ZSM-5 (**d**) samples (assessed at a methanol conversion of 60–90%). **e**, Ratio of ethylene to 2MBu for the four set of samples (see Supplementary Fig. 10 for changes in selectivity with TOS). **f**,**g**, Operando UV–vis diffuse reflectance spectroscopy after 4 h TOS for H-ZSM-11 (**f**) and H-ZSM-5 (**g**) catalysts at the same reaction conditions (see Supplementary Fig. 11 for data at earlier times). The shaded regions correspond to distinct hydrocarbon species. a.u., arbitrary units. **h**,**i**, TEM images and SAED patterns of a typical commercial zeolite H-ZSM-5 crystal (Zeolyst CBV5524G) (**h**) and a typical crystal of the corresponding finned material prepared by secondary growth (**i**) (see Supplementary Fig. 12 for additional images). Scale bars, 100 nm; inset scale bars, 5 nm^{-1}. **j**, TOS methanol conversion over as-received and finned commercial H-ZSM-5 during the MTH reaction at 350 °C with WHSV = 9 h^{-1}. The physicochemical properties of the samples in **a**–**g** and **h**–**j** are provided in Supplementary Tables 3 and 5, respectively.

a self-pillared pentasil (SPP) zeolite, which consists of intergrown few-nanometre-thick MFI nanosheets (that is, it has a uniform micro- and mesopore hierarchical structure throughout each particle), and as such it should exhibit only one (fast) timescale. Indeed, we obtained one diffusion regime, albeit somewhat slower than the fast one obtained in the finned samples, which indicates possible contributions of mesopore resistances in the SPP zeolite (Fig. 4f). Molecular dynamics simulations also confirmed that TMPyr is of sufficient size to fit within the channels of both MEL (Fig. 4g) and MFI (Supplementary Fig. 19) frameworks (see Supplementary Note 3 for more details).

Experimental points in TMPyr titration curves (see Supplementary Fig. 20 for details) were fitted using an exponential model (see Supplementary Note 2 for additional details) to obtain time constants for fast (τ_{fast}) and slow (τ) diffusion within the finned and interior micropore regions, respectively (Table 1). The finned

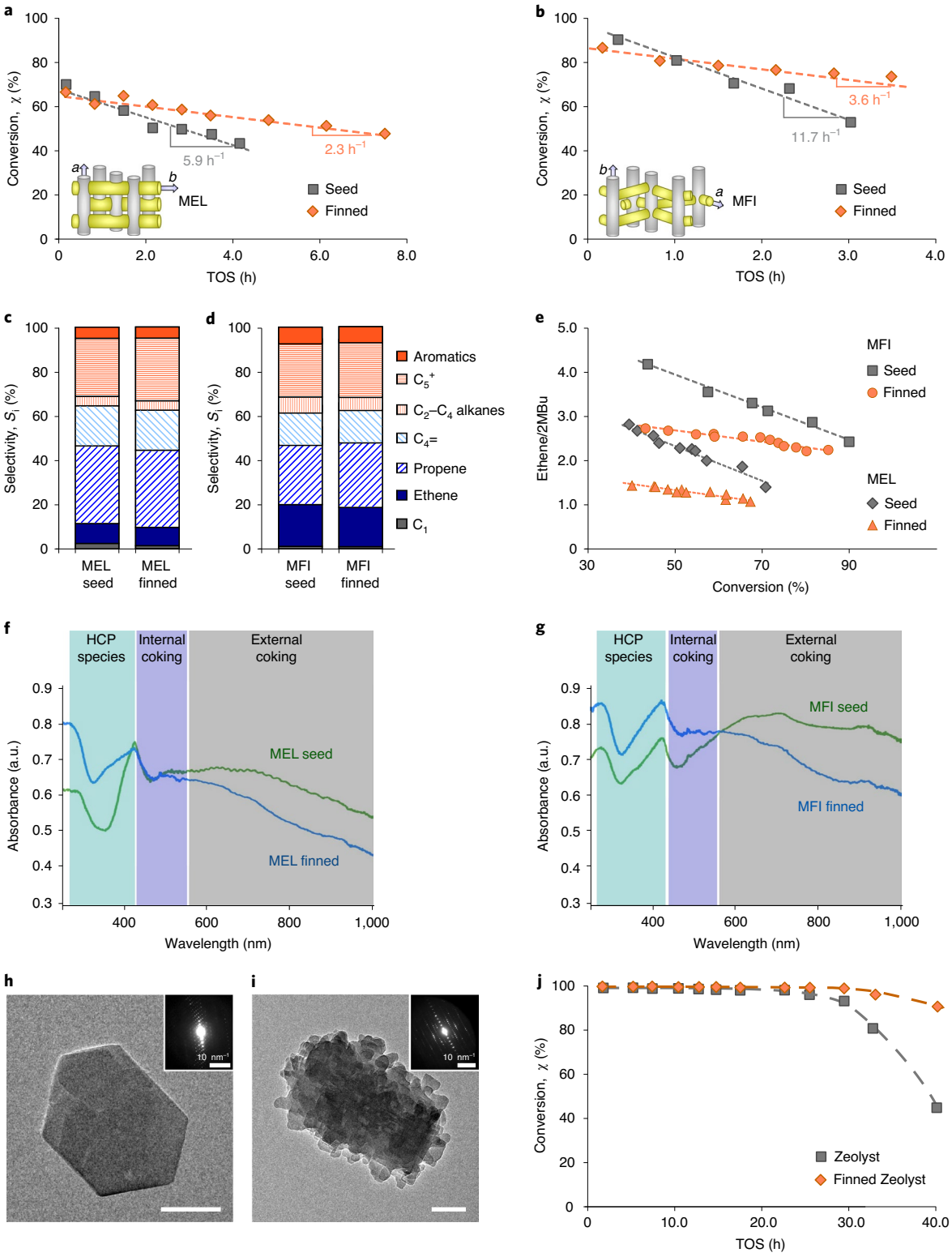

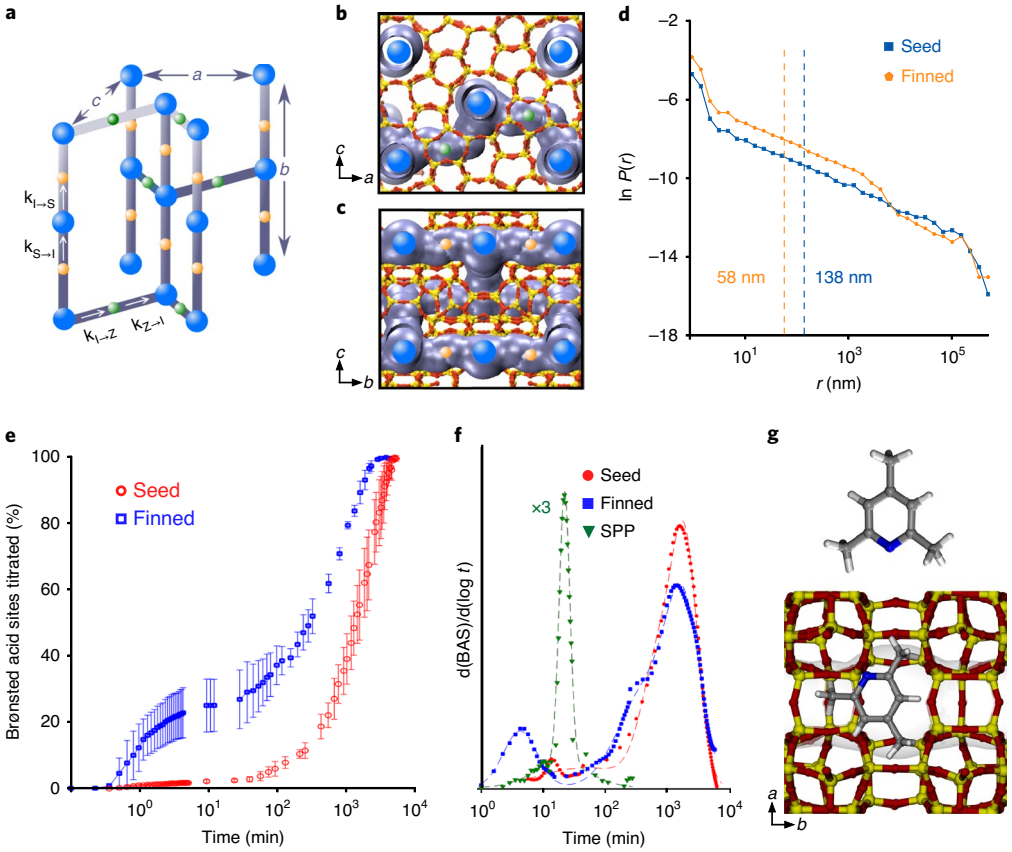

Fig. 4 | Enhanced mass-transport properties of finned zeolites. a–c, Molecular simulations of benzene diffusion in a finned Si-MFI structure. **a**, KMC lattice representation of the pore network for the MFI unit cell. Favourable adsorption sites in S, Z and I are labelled as orange, green and blue spheres, respectively. Kinetic constants $k_{i\rightarrow j}$ are the rates associated with the diffusive hopping of benzene from adsorption site *i* to *j* (Supplementary Table 6). **b**,**c**, Renderings along the *b* direction (**b**) and *a* direction (**c**) showing the KMC pore network superimposed on an atomistic unit cell. **d**, Log probability density distribution of the benzene diffusion path length *r* for a finned zeolite ($\beta = 500$, $\alpha = 50$ and $\gamma = 10$ nm; Fig. 1a) and a seed crystal with a cubic geometry ($\beta = 500$ nm). The dashed vertical lines mark the mean *r* values of 58 and 138 nm for the finned and seed crystals, respectively. **e**,**f**, Time-resolved titration of Brønsted acid sites (BAS) by TMPyr monitored by FTIR spectroscopy. **e**, Time-resolved titration of Brønsted acid sites for H-ZSM-11 seed and finned samples. **f**, Differential plot of titrated Brønsted acid sites in Zeolyst ZSM-5 (MFI type) seed and finned samples and SPP zeolite, with plots of additional samples shown in Supplementary Fig. 18 and the peak-fitting procedure shown in Supplementary Fig. 21. **g**, TMPyr structure and a snapshot from a molecular dynamics simulation (Supplementary Video 4) showing TMPyr within a MEL channel (see Supplementary Fig. 19 and Supplementary Video 5 for TMPyr in MFI).

Table 1 | Diffusion time constants from TMPyr titration

Sample	τ_{fast} (s)	τ (s)
MEL seed	–	6.6×10^5
MEL finned	2.4×10^2	6.7×10^4
MFI seed	–	2.6×10^5
MFI finned	4.4×10^2	1.2×10^5
Zeolyst	–	4.5×10^4
Finned Zeolyst	3.1×10^2	4.2×10^4
SPP	1.7×10^3	–

zeolites exhibit an initial rapid uptake kinetics three orders of magnitude faster than the seed. These trends are qualitatively consistent with KMC models and catalytic studies, which show distinct transport properties of finned zeolites in which the introduction of protrusions with size $\alpha << \beta$ markedly reduced the internal diffusion limitations. Time-resolved titration measurements also reveal that this disparity in time constants is maintained for nanocrystals in which the differences between α and β are less substantial (for example, Zeolyst H-ZSM-5 in Fig. 3h,i).

There are few synthesis methods capable of producing ZSM-5 and ZSM-11 crystal sizes in the range 10–80 nm. Conversely, methods to produce 2D crystals with sizes <10 nm often result in insufficient acid-site density (for example, Si/Al > 40) for industrial hydrocarbon catalysis. Moreover, ultrasmall crystallite sizes pose practical challenges for solids extraction in commercial synthesis processes. The generation of finned zeolites overcome these restrictions and challenges by altering the performance of large crystals to behave as pseudo-nanocrystals. Using a synergistic combination of state-of-the-art experimental techniques, we show that finned ZSM-5 and ZSM-11 zeolites possess unusually outstanding mass-transport properties. Markedly enhanced rates of molecular uptake in fins, coupled with reduced internal diffusion path lengths, leads to less coke formation on external surfaces, longer catalyst lifetimes and a shift in the product selectivities that are characteristic of zeolites with an overall crystal size equal to that of the average fin dimension. The ability to introduce fins through a facile secondary growth process is an alternative method to reduce diffusion limitations in zeolites. Here we demonstrate that this approach can be

used to enhance the performance of commercial catalysts, with the promise of becoming a generalized platform for the rational design of zeolites across a broad range of framework types.

Online content

Any methods, additional references, Nature Research reporting summaries, source data, extended data, supplementary information, acknowledgements, peer review information; details of author contributions and competing interests; and statements of data and code availability are available at https://doi.org/10.1038/s41563-020-0753-1.

Received: 6 February 2020; Accepted: 30 June 2020;
Published online: 10 August 2020

References

1. Gallego, E. M. et al. 'Ab initio' synthesis of zeolites for preestablished catalytic reactions. *Science* **355**, 1051–1054 (2017).
2. Paolucci, C. et al. Dynamic multinuclear sites formed by mobilized copper ions in NO_x selective catalytic reduction. *Science* **357**, 898–903 (2017).
3. Cychosz, K. A., Guillet-Nicolas, R., Garcia-Martinez, J. & Thommes, M. Recent advances in the textural characterization of hierarchically structured nanoporous materials. *Chem. Soc. Rev.* **46**, 389–414 (2017).
4. Varoon, K. et al. Dispersible exfoliated zeolite nanosheets and their application as a selective membrane. *Science* **333**, 72–75 (2011).
5. Rangnekar, N., Mittal, N., Elyassi, B., Caro, J. & Tsapatsis, M. Zeolite membranes—a review and comparison with MOFs. *Chem. Soc. Rev.* **44**, 7128–7154 (2015).
6. Karwacki, L. et al. Morphology-dependent zeolite intergrowth structures leading to distinct internal and outer-surface molecular diffusion barriers. *Nat. Mater.* **8**, 959–965 (2009).
7. Hwang, A. et al. Effects of diffusional constraints on lifetime and selectivity in methanol-to-olefins catalysis on HSAPO-34. *J. Catal.* **369**, 122–132 (2019).
8. Awala, H. et al. Template-free nanosized faujasite-type zeolites. *Nat. Mater.* **14**, 447–451 (2015).
9. Choi, M. et al. Stable single-unit-cell nanosheets of zeolite MFI as active and long-lived catalysts. *Nature* **461**, 246–249 (2009).
10. Na, K. et al. Directing zeolite structures into hierarchically nanoporous architectures. *Science* **333**, 328–332 (2011).
11. Zhang, X. et al. Synthesis of self-pillared zeolite nanosheets by repetitive branching. *Science* **336**, 1684–1687 (2012).
12. Mintova, S. et al. Nanosized microporous crystals: emerging applications. *Chem. Soc. Rev.* **44**, 7207–7233 (2015).
13. Gallego, E. M. et al. Simple organic structure directing agents for synthesizing nanocrystalline zeolites. *Chem. Sci* **8**, 8138–8149 (2017).
14. Vicente, J. et al. Direct synthesis of nano-ferrierite along the 10-ring-channel direction boosts their catalytic behavior. *Angew. Chem. Int. Ed.* **57**, 3459–3463 (2018).
15. Li, K., Valla, J. & Garcia-Martinez, J. Realizing the commercial potential of hierarchical zeolites: new opportunities in catalytic cracking. *ChemCatChem* **6**, 46–66 (2014).
16. Perez-Ramirez, J., Christensen, C. H., Egeblad, K., Christensen, C. H. & Groen, J. C. Hierarchical zeolites: enhanced utilisation of microporous crystals in catalysis by advances in materials design. *Chem. Soc. Rev.* **37**, 2530–2542 (2008).
17. Liu, Y. et al. Steam-stable aluminosilicate mesostructures assembled from zeolite type Y seeds. *J. Am. Chem. Soc.* **122**, 8791–8792 (2000).
18. Park, D. H. et al. Selective petroleum refining over a zeolite catalyst with small intracrystal mesopores. *Angew. Chem. Int. Ed.* **48**, 7645–7648 (2009).
19. Shen, Y. et al. Deconvoluting the competing effects of framework topology and diffusion path length on methanol-to-hydrocarbons reactions. *ACS Catal.* **8**, 11042–11053 (2018).
20. Ristanovic, Z. et al. Intergrowth structure and aluminium zoning of a zeolite ZSM-5 crystal as resolved by synchrotron-based micro X-Ray diffraction imaging. *Angew. Chem. Int. Ed.* **52**, 13382–13386 (2013).
21. Ding, K. et al. Constructing hierarchical porous zeolites via kinetic regulation. *J. Am. Chem. Soc.* **137**, 11238–11241 (2015).
22. De Yoreo, J. J. et al. Crystallization by particle attachment in synthetic, biogenic, and geologic environments. *Science* **349**, aaa6760 (2015).
23. Lupulescu, A. I. & Rimer, J. D. In situ imaging of silicalite-1 surface growth reveals the mechanism of crystallization. *Science* **344**, 729–732 (2014).
24. Zhu, H., Liu, Z., Kong, D., Wang, Y. & Xie, Z. Synthesis and catalytic performances of mesoporous zeolites templated by polyvinyl butyral gel as the mesopore directing agent. *J. Phys. Chem. C* **112**, 17257–17264 (2008).
25. Zhang, H. et al. Seeding bundlelike MFI zeolite mesocrystals: A dynamic, nonclassical crystallization via epitaxially anisotropic growth. *Chem. Mater.* **29**, 9247–9255 (2017).
26. Kim, S., Park, G., Woo, M. H., Kwak, G. & Kim, S. K. Control of hierarchical structure and framework–Al distribution of ZSM-5 via adjusting crystallization temperature and their effects on methanol conversion. *ACS Catal.* **9**, 2880–2892 (2019).
27. Ghorbanpour, A., Gumidyala, A., Grabow, L. C., Crossley, S. P. & Rimer, J. D. Epitaxial growth of ZSM-5@silicalite-1: a core-shell zeolite designed with passivated surface acidity. *ACS Nano* **9**, 4006–4016 (2015).
28. Ilias, S. & Bhan, A. Mechanism of the catalytic conversion of methanol to hydrocarbons. *ACS Catal.* **3**, 18–31 (2013).
29. Khare, R., Millar, D. & Bhan, A. A mechanistic basis for the effects of crystallite size on light olefin selectivity in methanol-to-hydrocarbons conversion on MFI. *J. Catal.* **321**, 23–31 (2015).
30. Nordvang, E. C., Borodina, E., Ruiz-Martinez, J., Fehrmann, R. & Weckhuysen, B. M. Effects of coke deposits on the catalytic performance of large zeolite H-ZSM-5 crystals during alcohol-to-hydrocarbon reactions as investigated by a combination of optical spectroscopy and microscopy. *Chem. Eur. J.* **21**, 17324–17335 (2015).
31. Kolokathis, P. D. et al. Dimensionality reduction of free energy profiles of benzene in silicalite-1: calculation of diffusion coefficients using transition state theory. *Mol. Simul.* **40**, 80–100 (2014).
32. Ruthven, D. M., Eic, M. & Richard, E. Diffusion of C_8 aromatic hydrocarbons in silicalite. *Zeolites* **11**, 647–653 (1991).
33. Góra-Marek, Kinga, Tarach, Karolina & Choi, Minkee 2,6-Di-*tert*-butylpyridine sorption approach to quantify the external acidity in hierarchical zeolites. *J. Phys. Chem. C* **118**, 12266–12274 (2014).

Methods

Seed-directed synthesis of finned ZSM-11 and ZSM-5 crystals. The ZSM-11 sample used as seeds was prepared with a molar composition of 10 DAO (1,8-diaminooctane):10 K_2O:100 SiO_2:1 Al_2O_3:4,000 H_2O. In a typical synthesis, 0.185 g of $Al_2(SO_4)_3$ was added to a mixture of 0.61 g of KOH solution (50 wt%) and 15.35 g of deionized water. To this solution was added 0.40 g of DAO, followed by 5.45 g of colloidal silica (LUDOX AS-30) and 0.22 g of calcined ZSM-11 crystals (2 wt%) according to the procedures outlined in a previous paper[34]. The resulting mixture was stirred at room temperature for 24 h. The sol gel was then placed in a 60 ml Teflon-lined acid digestion bomb and heated in an oven at 160 °C and autogenous pressure for 3 days. The crystalline product was removed from the mother liquor by three cycles of centrifugation and washes with deionized water, using a Beckman Coulter Avanti J-E centrifuge at 5 °C and 13,000 rpm for 10 min per cycle. The resulting seeds were immediately stored in deionized water without allowing time for the solids to dry. A seeded growth solution was made with a molar composition of 27.3 DAO:11.9 K_2O:90 SiO_2:0.5 Al_2O_3:3,588 H_2O. The solution was prepared by adding an appropriate amount of $Al_2(SO_4)_3$ to a solution that contained KOH and deionized water, followed by the addition of DAO and LUDOX AS-30. The mixture was stirred at room temperature for 24 h prior to adding 0.65 g of as-synthesized ZSM-11 seeds (10 wt% relative to the total amount of growth solution). The seeds were not calcined and contained occluded DAO. The suspension was heated for 2 days at 120 °C. The solids were extracted from the mother liquor using the centrifuge/washing procedure described above. ZSM-5 seeds and finned samples were prepared by a similar protocol (see Supplementary Information for details).

Characterization. The H-forms of the zeolite materials were characterized by powder XRD using a Rigaku SmartLab Diffractometer with Cu Kα radiation to verify the crystalline structure. Powder XRD patterns were compared to simulated patterns of each framework type provided by the International Zeolite Association Structure Database[35]. Textural analysis of the H-form samples prepared for catalytic testing was performed by N_2 adsorption/desorption using a Micromeritics ASAP 2020. The data were analysed by instrument software to obtain the Brunauer–Emmett–Teller surface area and the microporous volume was determined from the *t*-plot method.

TEM images and SAED patterns were taken with a JEOL JEM-2100 FEG TEM operated at an accelerating voltage of 200 kV. A Gatan Ultrascan CCD (charge-coupled device) camera was used to collect image data and a Gatan Orius 200D CCD detector was used to collect diffraction data. Sample particles were dispersed and ultrasonicated in ethanol and then dipped on a lacey carbon copper grid. Electron tomography was also performed using the JEOL JEM-2100 FEG. A Gatan 912 ultrahigh tilt tomography sample holder was used to achieve a large tilt range. A tilt series of bright-field TEM images of a zeolite crystal particle was acquired over an angular range from −65 to +65°. The interval between neighbouring images was kept at 1.0°. Before the sample was placed on the copper grid, a droplet of a 5 nm gold nanoparticle dispersion was also delivered onto the copper grid as a fiducial marker for tomogram alignment. The software ETomo was used for tilt series data processing, which included alignment and reconstruction.

MTH reactions. The MTH reaction was carried out according to a previously reported procedure[19] using a fixed-bed stainless-steel reactor (inner diameter = 1/4 inch (6.35 mm)), H-form zeolite catalysts and a reaction temperature of 350 °C (Thermo Scientific Lindberg Blue M furnace). The catalysts were pressed and sieved (40–60 mesh) and then homogeneously mixed with a diluent (silica gel, 35–60 mesh; Sigma-Aldrich). Two plugs of quartz wool were used to support the catalyst bed and the reaction temperature was monitored by a K-type thermocouple (Omega Engineering) inserted into the stainless-steel tube. Prior to the reaction, the catalyst bed was activated in situ at 550 °C for 3 h under a flow of dried air and then cooled to 350 °C. Methanol (99.9% purity) was continuously fed into the reactor at a WHSV of 9 h^{-1} by a syringe pump (Harvard Apparatus) at 7 µl min^{-1} with a preheated inert gas stream of argon (30 cm^3 min^{-1}). The effluent was analysed by an online gas chromatograph (Agilent GC7890A) equipped with a flame ionization detector. To compare the deactivation rate of the catalysts, reactions were carried out at a subcomplete methanol conversion, *X*, with the initial conversion regulated by adjusting the catalyst mass. Methanol conversion is defined as:

$$X = \left[1 - \left(\frac{C_{\text{eff}}}{C_{\text{feed}}}\right)\right] \times 100\% \quad (1)$$

where C_{eff} is the carbon-based molar concentration of both methanol and dimethyl ether measured in the effluent and C_{feed} is the concentration of methanol measured in the feed. The selectivity, S_i, of hydrocarbon product *i* is defined as:

$$S_i = \left(\frac{C_i}{C_{\text{t,eff}}}\right) \times 100\% \quad (2)$$

where C_i is the carbon-based molar concentration of hydrocarbon *i* measured in the effluent and $C_{\text{t,eff}}$ is the total carbon-based molar concentration of hydrocarbons measured in the effluent.

Operando UV−vis diffuse reflectance microscopy. The reaction intermediates and coke species formed during the MTH reactions were monitored by operando UV–vis diffuse reflectance spectroscopy using an AvaSpec 2048 L spectrometer[36,37]. The UV–vis spectra were collected in the wavelength range 200–1,000 nm (11,000–50,000 cm^{-1} in wavenumber) in reflection mode using a high-temperature UV–vis optical fibre probe (Avantes). The probe was placed in a stainless-steel protection sleeve and comprised one excitation and one collection optical fibre with a diameter of 400 µm and a length of 1.5 m. Typically, catalysts with the same pellet size to the performance testing were loaded in a fixed-bed quartz reactor (inner diameter = 6 mm × 3 mm) and activated at 550 °C for 3 h under 100% oxygen and then cooled to 350 °C (for the reaction) under a flow of helium. A WHSV of 20 h^{-1} was obtained for methanol by flowing helium gas through a methanol saturator at ~25 °C. UV–vis spectra were collected and saved every 30 s with 100 accumulations.

FTIR spectroscopy. Time-resolved spectra were measured using a Bruker Vertex 70 FTIR with a HeNe laser and RT-DLaTGS detector (20 kHz scanner velocity, 6 mm aperture and KBr beam splitter). For the sample preparation, ~15 mg of a powder catalyst sample was homogenized using an agate mortar and pestle, pressed at 2–3 ton (CrushIR Digital Hydraulic Press; Pike Technologies) for 5 min into 13-mm-diameter pellets (KBR Die, CAS no. 7758-02-3; International Crystal Laboratories) and inserted into the cell body (high temperature cell, Part no. HTC-M-05, CaF_2 windows; Harrick Scientific). Before inserting the sample pellet, a background spectrum was collected (64 scans at 4 cm^{-1} resolution) with the empty cell. A K-type thermocouple (Part no. 008–144; Harrick Scientific) was in constant intimate contact with the sample pellet holder. The manufacturer-provided cartridge heater (100 W, 24 V) was controlled via a temperature controller in cascade mode (Omega CN7800). To ensure that the CaF_2 windows of the sample cell do not overheat, cooling water was continuously pumped (variable flow chemical pump; Control Company) and flowed through water-cooling ports connected to the cell body. The sample was calcined at 500 °C for 4 h in air (Air Ultra Zero; Linde) at a ramp rate of 5 °C min^{-1}. After calcination, the sample was cooled down to and remained at 150 °C for the duration of the experiment to ensure the absence of water. For the amine purification, H-ZSM-5 (CBV28014; Zeolyst International) was calcined under flowing air at 550 °C for 10 h at a ramp rate of 1 °C min^{-1}. Freshly calcined H-ZSM-5 was added to 20 ml of TMPyr and stirred vigorously (1,200 r.p.m.) for >1 h. H-ZSM-5 was isolated from TMPyr via centrifugation at 10,000 r.p.m. for >5 min. TMPyr was used immediately postpurification for dosing in FTIR. For the amine dosing process, He gas was flowed over the sample pellet to purge any remaining air. To ensure that the He was moisture-free, He gas was flowed through a liquid nitrogen trap and desiccator before reaching the cell body. The initial spectrum of the calcined catalyst was measured at this time, with the background spectrum subtracted. Purified TMPyr was flowed at 0.06 ml h^{-1} to the sample cell. FTIR spectra (64 scans, 4 cm^{-1} resolution and scan range from 4,000 to 1,000 cm^{-1}) were saved continuously at different time intervals during the duration of the experiment: every 30 s for the first 10 min, then every 30 min for the rest of the experiment.

KMC simulations. KMC simulations were performed to study the transport of benzene through seed and finned silicalite-1 crystals at 300 K. Benzene transport in silicalite-1 was characterized by infrequent jumps between three types of favourable adsorption sites located in S, Z and I of the pores (Fig. 4a–c). This hopping process was modelled using first-order kinetic equations solved stochastically using the rejection-free KMC algorithm described by Laloué et al.[38]. The rate constants for the elementary transitions between adsorption sites (Supplementary Table 6) were derived in a previous atomistic simulation study using rare-event sampling methods, in which they were shown to lead to good predictions of benzene's experimentally measured diffusivity[31,39].

The seed and finned zeolite crystals were created by replication of the orthorhombic (*Pnma*) unit cell of MFI, which has unit-cell dimensions of $a = 2.01$ nm, $b = 1.99$ nm and $c = 1.34$ nm along its three principal crystallographic axes. The seed crystal was generated by replicating the unit cell to create a nearly cubic 247 × 250 × 372 (496.47 × 497.50 × 498.48 nm^3) supercell with linear dimensions of about $\beta = 500$ nm in each direction (Fig. 1a). The finned crystal was generated by decorating the surface of the smooth structure with smaller, nearly cubic 24 × 25 × 37 (48.24 × 49.750 × 49.58 nm^3) supercells with linear dimensions of $\alpha = 50$ nm in each direction; the fin location on the surface was chosen to ensure continuity of the pore network. As prescribed by the KMC model, the pore networks of both crystals were represented as lattices with S, Z, and I adsorption sites (Fig. 4a–c). On the order of 10^8 and 10^9 lattice sites were needed to represent the seed and finned structures, respectively, examined in this study.

Mass transport through the seed and finned zeolite crystals was characterized by computing the diffusion path length for benzene:

$$r = \sum_{i=1}^{n-1} |\Delta \mathbf{r}_i| \quad (3)$$

where $|\Delta \mathbf{r}_i| = |\mathbf{r}_i - \mathbf{r}_{i-1}|$ is the scalar distance travelled in the *i*th KMC step and $\mathbf{r}_i$ is the position vector of the molecule. The initial position $\mathbf{r}_0$ at time $t_0 = 0$ was chosen by placing benzene at a randomly selected lattice site on the outside of

the crystal's bounding surface. The KMC moves were attempted and rejected until the molecule first crossed the bounding surface of the crystal to enter at position $\mathbf{r}_1$ and time t_1. The trajectory of the molecule was then propagated for n KMC steps, with the nth step corresponding to the event in which the molecule first exited the zeolite crystal by recrossing the bounding surface. The residence time within the crystal was calculated as $\tau = t_{n-1} - t_1$. For each structure, the mean diffusion path length r and residence time τ were estimated by averaging over 10^5 independent trajectories. In each case, only a single benzene molecule was simulated inside the crystal such that interactions between diffusing species could be neglected.

Simulations were performed for several models with different surface-to-surface fin spacing γ, ranging from 4 to 50 nm to vary the surface density of fins from 3.27×10^{-4} to 1.01×10^{-4} nm^{-2} (Supplementary Table 7). The mean diffusion path length r and residence time τ decrease monotonically as the surface density of the fins increases. For the models examined, these metrics were reduced by a factor that ranged from 1.5 to 2.5, and thereby demonstrated that the mass-transport characteristics of the finned crystals were enhanced relative to those of the seed zeolites for a broad range of fin densities.

Data availability

The data represented in Table 1 and Figs. 1, 3 and 4 of the manuscript, Supplementary Figs. 2, 5–11, 13, 15–18 and 20, and Supplementary Tables 1, 3, 5 and 7 are provided as Source data with this paper. Additional data related to the paper may be requested from the authors.

References

34. Shen, Y., Le, T. T., Li, R. & Rimer, J. D. Optimized synthesis of ZSM-11 catalysts using 1,8-diaminooctane as a structure-directing agent. *ChemPhysChem* **19**, 529–537 (2018).
35. International Zeolite Association (IZA) Structure Database. *IZA* http://www.iza-structure.org/databases/ (2017).
36. Borodina, E. et al. Influence of the reaction temperature on the nature of the active and deactivating species during methanol to olefins conversion over H-SSZ-13. *ACS Catal.* **5**, 992–1003 (2015).
37. Yarulina, I. et al. Structure-performance descriptors and the role of Lewis acidity in the methanol-to-propylene process. *Nat. Chem.* **10**, 804–812 (2018).
38. Laloué, N., Laroche, C., Jobic, H. & Methivier, A. Kinetic Monte Carlo study of binary diffusion in silicalite. *Adsorption* **13**, 491–500 (2007).
39. Forester, T. R. & Smith, W. Bluemoon simulations of benzene in silicalite-1 - Prediction of free energies and diffusion coefficients. *J. Chem. Soc. Faraday Trans.* **93**, 3249–3257 (1997).

Acknowledgements

J.D.R. acknowledges support primarily from the US Department of Energy, Office of Science, Office of Basic Energy Sciences (award DE-SC0014468). J.D.R. and J.C.P. acknowledge funding from the Welch Foundation (award nos. E-1794 and E-1882, respectively). X.Z. received funding from the Swedish Research Council (award no. 2017-0432) and the Knut and Alice Wallenberg Foundation (award no. 2012.0112). P.J.D. and M.T. received funding from the Catalysis Center for Energy Innovation, a US Department of Energy—Energy Frontier Research Center under Grant DE-SC0001004. B.M.W. acknowledges financial support from a European Research Council (ERC) Advanced Grant (no. 321140) and the Netherlands Organization for Scientific Research (NWO) Gravitation Program (Netherlands Center for Multiscale Catalytic Energy Conversion, MCEC) funded by the Ministry of Education, Culture and Science of the government of the Netherlands. J.C.P. received additional funding from the National Science Foundation (award CBET-1629398). We thank P. Kumar for assistance with XRD analysis.

Author contributions

J.D.R. and Y.S. conceived the project and designed the experiments. H.D., T.Y., C.L., D.F., A.A. and T.T.L. were primarily responsible for the data collection and analysis. X.Z. and B.M.W. were responsible for TEM and operando UV–vis measurements, respectively. P.J.D. and M.T. were responsible for the TMPyr titration measurements. J.C.P. conducted the computational studies. J.D.R. was responsible for the zeolite synthesis, characterization and catalytic testing. J.D.R. and H.D. wrote the manuscript and prepared the figures with help from the other co-authors. All the authors contributed to the scientific discussions and preparation of the manuscript and Supplementary Information materials.

Competing interests

J.D.R., Y.S. and H.D. filed a provisional patent based on the concepts developed in this manuscript.

Additional information

Supplementary information is available for this paper at https://doi.org/10.1038/s41563-020-0753-1.

Correspondence and requests for materials should be addressed to J.D.R.

Reprints and permissions information is available at www.nature.com/reprints.